

Constraining High Speed Winds in Exoplanet Atmospheres Through Observations of Anomalous Doppler Shifts During Transit

Eliza Miller-Ricci Kempton

Department of Astronomy and Astrophysics, University of California, Santa Cruz, CA 95064

ekempton@ucolick.org

Emily Rauscher

Lunar and Planetary Laboratory, University of Arizona, 1629 East University Blvd., Tucson, AZ 85721

ABSTRACT

Three-dimensional (3-D) dynamical models of hot Jupiter atmospheres predict very strong wind speeds. For tidally locked hot Jupiters, winds at high altitude in the planet's atmosphere advect heat from the day side to the cooler night side of the planet. Net wind speeds on the order of 1-10 km/s directed towards the night side of the planet are predicted at mbar pressures, which is the approximate pressure level probed by transmission spectroscopy. These winds should result in an observed blue shift of spectral lines in transmission on the order of the wind speed. Indeed, Snellen et al. (2010) recently observed a 2 ± 1 km/s blue shift of CO transmission features for HD 209458b, which has been interpreted as a detection of the day-to-night winds that have been predicted by 3-D atmospheric dynamics modeling. Here we present the results of a coupled 3-D atmospheric dynamics and transmission spectrum model, which predicts the Doppler-shifted spectrum of a hot Jupiter during transit resulting from winds in the planet's atmosphere. We explore four different models for the hot Jupiter atmosphere using different prescriptions for atmospheric drag via interaction with planetary magnetic fields. We find that models with no magnetic drag produce net Doppler blueshifts in the transmission spectrum of ~ 2 km/s and that lower Doppler shifts of ~ 1 km/s are found for the higher drag cases, results consistent with — but not yet strongly constrained by — the Snellen et al. (2010) measurement. We additionally explore the possibility of recovering the average terminator wind speed as a function of altitude by measuring Doppler shifts of

individual spectral lines and spatially resolving wind speeds across the leading and trailing terminators during ingress and egress.

Subject headings: planetary systems

1. Introduction

Hot Jupiter exoplanets represent a fundamentally new class of planets that were not anticipated and are not present within our solar system. These planets exist in extreme environments, residing very close to their host stars at semi-major axes of several hundredths of an A.U. The mechanism that allows hot Jupiters to migrate in to the near vicinity of their host stars from a formation location that was presumably much further out beyond the snow line is still very much an open (and much debated) question. In general, hot Jupiters fundamentally extend our understanding of planet atmosphere, structure, evolution, and migration into a new regime, and therefore further study of these planets aimed at characterizing and understanding their current states is warranted.

In particular, hot Jupiters lie in a very interesting regime in terms of their atmospheric dynamics, in that they are expected to be tidally locked from simple timescale arguments (e.g. Rasio et al. 1996). This leads to the planets having permanent hot day sides and colder night sides. An important outstanding question is the extent to which heat is recirculated from the day side to the night side of these planets, which has important implications for their global energy budgets. Some constraints have been made on day-to-night heat redistribution on hot Jupiters by observing the planets' IR emission as a function of orbital phase (Harrington et al. 2006; Knutson et al. 2007; Cowan et al. 2007; Knutson et al. 2009; Crossfield et al. 2010). However, the patterns seem to vary strongly from planet to planet. More insight remains to be gained from additional observations of this type along with direct constraints on the winds in hot Jupiter atmospheres, which ultimately govern the day-to-night heat flow.

Three-dimensional models of the atmospheric dynamics of hot Jupiters have been presented by a number of authors (e.g. Showman et al. 2009; Dobbs-Dixon et al. 2010; Rauscher & Menou 2010; Heng et al. 2011; Thrastarson & Cho 2011), with the goal of understanding this new regime of atmospheric circulation. While these models can vary considerably in the treatment and level of complexity of the underlying physics, a number of the qualitative results on hot Jupiter atmospheric dynamics have proved to be robust across most of the models. These are (1) winds at pressures of ~ 1 bar set up an equatorial jet that moves in the direction of the planet's rotation (see Showman & Polvani 2011, for an analytic description

this behavior), (2) as a result of the equatorial wind pattern, the hottest point on the planet is shifted away from the substellar point in the direction of the planet’s rotation, and (3) winds higher in the atmosphere at \sim mbar pressures tend to flow directly from the hot day side to the cooler night side of the planet. These three characteristics of the atmospheric dynamics models comprise a set of predictions for hot Jupiter wind and temperature patterns that can ultimately be tested through observations of the planetary atmospheres. Already, observations constraining the brightness temperatures of certain hot Jupiters as a function of orbital phase have been found to be in general agreement with prediction (2) from the list above (Knutson et al. 2007, 2009). However, the observed magnitude of the hot-spot shift from the substellar point varies to a greater extent than predicted by the circulation models (Crossfield et al. 2010). Confirming the other two predictions – (1) and (3) – will ultimately require direct measurements of wind speeds in hot Jupiter atmospheres to confirm the nature of the winds themselves.

Recently Snellen et al. (2010) produced the first tentative detection of exoplanet winds in the atmosphere of the transiting hot Jupiter HD 209458b. Their measurement, if taken at face value, supports one of the theoretical model predictions of the wind flow pattern in hot Jupiter atmospheres – that high altitude winds should be directed towards the night side of the planet. Snellen et al. (2010) obtained a high resolution transmission spectrum of HD 209458b, revealing the excess absorption of stellar light through the planet’s atmosphere during transit. At their high spectral resolution of $\sim 10^5$ using the CRIRES spectrograph on the VLT, the authors were able to detect Doppler shifts in the planet’s absorption lines during transit. A linear drift in velocity was detected throughout transit, which was attributed to the orbital velocity of the planet of 140 ± 10 km s $^{-1}$. This direct detection of the planet’s motion allowed for a direct measurement of the planet’s mass, matching previous inferences of the planetary mass from stellar radial velocities (RVs). Interestingly, when the Doppler signature of the orbital motion was subtracted off, Snellen et al. (2010) found a remaining systematic 2 ± 1 km s $^{-1}$ blueshift in the planet’s absorption signature. This remaining blueshift has been attributed to the high-altitude winds in HD 209458b’s atmosphere, as predicted by theoretical atmospheric dynamics modeling. These high-altitude winds should be directed towards the night side of the planet (and therefore directly towards the observer) at the \sim mbar pressure level probed by transmission spectroscopy, consistent with the observed net blueshift in the transmission spectrum. In addition to the Snellen et al. (2010) result, substantial blueshifts have now been detected in the the optical transmission spectra of several other transiting planets (Redfield et al. 2008; Jensen et al. 2011), which might result from a combination of orbital motion along with high-speed winds, but the implications of these observations have not been fully studied.

The interpretation of the Snellen et al. (2010) result as a direct detection of high-altitude

winds in the atmosphere of HD 209458b is compelling, but requires further scrutiny. Atmospheric dynamics models tend to produce wind speeds of $\sim 1\text{--}10\text{ km s}^{-1}$ at mbar pressure levels (Showman et al. 2009; Dobbs-Dixon et al. 2010; Rauscher & Menou 2010; Heng et al. 2011), directed towards the night side of tidally-locked hot Jupiters. Interestingly, these wind speeds could be significantly reduced by magnetic effects at work in the planet’s atmosphere. The upper atmosphere is hot enough to be weakly thermally ionized and, assuming a planetary magnetic field, the flow of the charged winds will induce a new component of the magnetic field with associated currents. The winds will experience a drag – Perna et al. (2010) show that this magnetic drag could potentially be strong enough to reduce zonal wind speeds by up to a factor of ~ 3 and alter the flow structure.

Still, it is not straightforward to translate these wind speeds into the transmission spectral signature of a hot Jupiter atmosphere. In this paper we attempt to do just that. We couple together an existing 3-D atmospheric dynamics model (Rauscher & Menou 2010; Perna et al. 2010) with a transmission spectroscopy code (Miller-Ricci et al. 2009; Miller-Ricci & Fortney 2010) such that the 3-D temperature-pressure and wind speed structures are self-consistently treated in the transmission radiative transfer. The end result is to produce Doppler-shifted transmission spectra that include the effects of velocity shifts due to winds along with planetary rotation and orbital motion on the planet’s absorption features. Previous work by Spiegel et al. (2007) studied the velocity effects of rotation on the transmission spectra of exoplanets but did not include the more dominant effect of winds. Our work also goes beyond previous work coupling 3-D atmospheric dynamics and radiative transfer models, which have self-consistently treated the temperature-pressure structure with the radiative transfer, while neglecting the Doppler shift inducing effect of winds (Fortney et al. 2010; Burrows et al. 2010).

Our goal is to determine whether measurements of Doppler shifted winds in hot Jupiter atmospheres during transit could be used to constrain the nature of the wind patterns themselves. Furthermore, we attempt to determine whether a 2 km s^{-1} blueshift, as seen in the Snellen et al. (2010) transmission spectrum of HD 209458b, is consistent with the results of the atmospheric dynamics modeling. Specifically, we look at dynamics models that use different prescriptions for the treatment of drag in the atmospheres of hot Jupiters. We study cases with no additional sources of atmospheric drag along with cases where prescriptions for magnetic drag have been included, to determine the overall effect on the planetary wind patterns as well as how these assumptions can alter the transmission signature of such a planet. We also look into the possibility of recovering the spatial structure of exoplanet winds through transmission spectroscopy, both by using individual spectral lines to probe different heights in the planet’s atmosphere and by measuring Doppler shifts during transit ingress and egress to separately map out wind speeds across the planet’s eastern and western

terminators.

We present our model and methodology in Section 2. Our transmission spectrum results are presented in Section 3. Finally, we offer up some summarizing thoughts and conclusions in Section 4.

2. Methodology

2.1. 3-D Dynamics Models

We present four models of hot Jupiter circulation here, two that are drag-free and two that include a simple treatment of magnetic drag in the atmosphere. The drag-free models differ in that one uses the same hyperdissipation strength from Rauscher & Menou (2010), while the other uses a hyperdissipation timescale an order of magnitude shorter in order to reduce the numerical noise that is apparent at low pressures in the original model. The two magnetic drag models differ in the implementation of drag at low pressures, as discussed below. The three-dimensional models analyzed in this paper are all basic extensions of models presented previously in Rauscher & Menou (2010) and Perna et al. (2010), and details can be found in those papers. Briefly, they were all calculated using the same dynamical core and Newtonian relaxation scheme for radiative forcing as presented in Menou & Rauscher (2009). Each model was run for 2000 planet days at a resolution of T31L45 (corresponding to a horizontal resolution of $\sim 4^\circ$ and 45 vertical levels in log pressure). Two modifications have been made to the set-up of these models in order to better facilitate calculation of transmission spectra: a different specific gas constant was used and the upper boundary has been extended up to 10 μ bar.

The models from Rauscher & Menou (2010) and Perna et al. (2010) used a specific gas constant of $R = 4593 \text{ J K}^{-1} \text{ kg}^{-1}$, which corresponds to a mean molecular mass of 1.81 g/mol, and a value for R/c_p of 0.321 (c_p is the specific heat capacity at constant pressure). For better consistency with the transmission spectroscopy modeling, which is highly sensitive to atmospheric scale height and therefore mean molecular weight (e.g. Miller-Ricci et al. 2009), we chose to use $R = 3523 \text{ J K}^{-1} \text{ kg}^{-1}$ and $R/c_p = 0.286$ in the circulation models presented here. This now corresponds to a mean molecular weight of 2.36 g/mol, a value more appropriate for solar composition, while the value for R/c_p now matches that for a purely diatomic gas.

The other significant change over the previously published models is that we have extended the upper boundary of the atmosphere to 10 μ bar, necessary because transmission spectra probe pressures well above the 1 mbar top boundary of the original models. This

extension to lower pressures meant that we had to extrapolate our radiative forcing and drag prescriptions.

The Newtonian relaxation scheme used for the radiative forcing requires the choice of equilibrium temperatures and radiative times (for details see Rauscher & Menou 2010). In order to extend these up to 10 μ bar we chose to continue the 1000 K day-night temperature difference, which is constant down to 100 mbar. The night side temperature was then set in the same manner as in our previous work, so that at each level the integrated T^4 matched the profile from Figure 1 of Iro et al. (2005). The radiative times were taken from Figure 4 of Iro et al. (2005), which includes these lower pressures.

For a simplified treatment of magnetic drag in the atmospheres of hot Jupiters, the models presented in Perna et al. (2010) employed a Rayleigh drag with a time constant that is horizontally uniform, but varies with pressure: $dv/dt = -v/\tau_{\text{drag}}(P)$. Here we use the strongest drag strengths from Perna et al. (2010), which ranged from 2×10^4 s at 1 mbar to 8×10^6 s at 100 bar. Since this scheme is already simplifying the underlying physics of magnetic drag, we choose two simple forms for the extrapolation of drag times to lower pressure: either we maintain a constant τ_{drag} above 1 mbar, or we maintain a constant $\tau_{\text{drag}}/\tau_{\text{rad}}$ ratio above 1 mbar. Figure 1 shows the radiative and drag times used throughout our models.

To summarize the four atmosphere models, they are:

1. *Drag-Free*: Canonical hot Jupiter model from Rauscher & Menou (2010), but extended to an upper boundary at 10 μ bar and using an updated gas constant.
2. *Drag-Free + Hyperdissipation*: Same as the drag-free model but with a hyperdissipation timescale that is an order of magnitude shorter to reduce numerical noise in the model.
3. *Magnetic Drag (a)*: Magnetic drag model using the strongest drag strengths from Perna et al. (2010) below 1 mbar and maintaining a constant τ_{drag} above 1 mbar.
4. *Magnetic Drag (b)*: Same as magnetic drag model (a) but with a constant $\tau_{\text{drag}}/\tau_{\text{rad}}$ ratio above 1 mbar. Since this means that the drag timescale continues to decrease with pressure, this model experiences stronger drag than model (a).

The atmospheric structure for all four models is qualitatively very similar to the results presented in Rauscher & Menou (2010) and Perna et al. (2010). High in the atmosphere the basic flow pattern is from the hot day side to the cold night side, across all latitudes of the terminator, with transonic wind speeds (although weaker for the magnetic drag models).

At moderate pressures (hundreds of mbar) the advective timescales become comparable to the radiative timescales and the flow is able to alter the temperature structure from a hot-day/cold-night pattern to one where the hottest region of the atmosphere is advected eastward of the substellar point. Finally, at deep pressures the winds are much slower (and subsonic), but are easily able to minimize day-night temperature differences. Some details are different between the models analyzed here and those in Rauscher & Menou (2010) and Perna et al. (2010). While similar, the advected temperature structures are not identical. In addition, similar features between the models tend to occur at slightly lower pressure in the original models than the ones here, likely a result of the change in the specific gas constant and its effect on the pressure scale height.

The four models in this paper have generally similar temperature structures throughout the atmosphere, as shown by the temperature-pressure profiles in Figure 2. Although the behavior at high pressure varies between the drag and drag-free models, all of the models have the same day-night temperature difference at low pressures (due to the same radiative forcing set-up and very short radiative times). The models with magnetic drag or extra hyperdissipation do not show the effect of small-scale numerical noise seen in the original drag-free model. The temperature structure around the west terminator ($\theta = 270^\circ$) is nearly the same as the east terminator ($\theta = 90^\circ$) for the magnetic drag models, but has a profile that has been more altered by advection in the drag-free models.

The main difference between the four models is the flow structure, especially at the low pressures probed by transmission spectroscopy, where the Doppler effect could be observed. The differences between the high-altitude flow in our four models can be seen in more detail in Figure 3, which shows flow patterns across the planet at the $60 \mu\text{bar}$ level, representative of the high-altitude regime. In all cases the winds are directed away from the substellar point towards the anti-stellar point across the terminator. This results in a net blue-shifted wind directed towards the observer during transit for all models, although the magnitude of the wind speed and the details of the wind pattern vary from model to model.

First we compare the no-drag models. Enhanced hyperdissipation in the second drag-free model reduces the numerical build-up of noise on small scales, which has the effect of making the flow more coherent, but reduces the maximum wind speeds. Nevertheless, the mean eastward wind speed across the terminator is nearly the same for both models, and remains nearly identical between the two models across a wide range of pressures ($\sim 5 \text{ km s}^{-1}$ at $60 \mu\text{bar}$). The models with magnetic drag have much slower winds at this pressure. The flow in model (b) is strongest in a narrow region on either side of the terminator, which is also the area probed by transmission spectroscopy, but it has an average eastward wind speed at the terminator of only $\sim 2.3 \text{ km s}^{-1}$, compared to $\sim 3.8 \text{ km s}^{-1}$ in model (a).

The magnetic drag models have similar average terminator winds throughout much of the atmosphere (where they have identical drag times), but at pressures less than 1 mbar the winds in the weak-drag model increase with altitude, while the winds in the strong-drag model decrease.

2.2. Transmission Spectrum Radiative Transfer

The transmission spectrum is obtained by dividing the spectrum obtained during transit by the stellar spectrum, thus revealing the excess absorption from the species that make up the planetary atmosphere. We calculate the attenuation in intensity of a beam of stellar light passing through the planet’s atmosphere according to

$$I(\lambda) = I_0 e^{-\tau}, \quad (1)$$

where I_0 is the incident intensity from the star. We ignore any effects of additional scattering into or out of the beam or refraction, which have been found to be of minimal affect to hot Jupiter transmission spectroscopy (Hubbard et al. 2001) . The slant optical depth τ is calculated as a function of wavelength λ , height H , and latitude ϕ according to

$$\tau = \int \kappa ds, \quad (2)$$

where ds is the differential path length through the planet’s atmosphere along the observer’s line of sight, and κ is the opacity calculated for solar composition gas evaluated at the local temperature and pressure, which are each in turn dependent on the local height H , latitude ϕ , and longitude θ according to the 3-D dynamics model. The opacity is furthermore Doppler shifted by the local line-of-sight velocity as outlined in the following paragraphs. We include opacities from gas phase CH_4 , CO , CO_2 , H_2O , and NH_3 along with collision-induced H_2 opacities. Further details on our opacity tables and equilibrium chemistry calculations for solar composition gas can be found in Miller-Ricci et al. (2009) and Miller-Ricci & Fortney (2010). It is important to note for this work that our opacity tables of the molecular absorption come in the form of line lists, which allows us to calculate opacities at arbitrary spectral resolution. The total in-transit flux passing through the planet’s atmosphere is then calculated by integrating the intensity from Equation 1 over the solid angle subtended by the atmosphere.

As photons pass through the planetary atmosphere during transit, they encounter gas moving at the local velocity v , whose line-of-site component will induce a Doppler shift on the absorption signature. The Doppler shift through the planet’s atmosphere is given by

$$\frac{\Delta\lambda}{\lambda} = \frac{v_{LOS}}{c}, \quad (3)$$

where v_{LOS} is the line-of-sight component of the velocity. There are three components that contribute to the line-of-sight velocity that a photon “sees” as it passes through the planet’s atmosphere. These are (1) the wind speed, (2) the rotational velocity, and (3) the orbital speed, all evaluated locally in the planet’s atmosphere. The net line of sight component to the velocity is then given by

$$v_{LOS} = -(u \sin \theta \cos \phi + v \cos \theta \sin \phi + (R_p + z)\Omega \sin \theta \cos \phi + v_{orb} \sin \varphi). \quad (4)$$

The first two terms in Equation 4 give the contribution to the line-of-sight velocity from the winds in the planet’s atmosphere. The east-west and north-south components of the wind are given by u and v , respectively. The third term in the equation gives the contribution from the planet’s rotation, where R_p is the planet’s radius at 1 bar ($= 1.32 R_{Jup}$ for all models), z is the height in the atmosphere above the 1-bar level, and Ω is the planet’s rotational speed in radians s^{-1} . The final term in Equation 4 gives the contribution from the orbital motion of the planet. The orbital speed is denoted by v_{orb} , and φ is the phase angle of the orbit, defined as $\varphi = 0$ at the center of transit. For the results presented in this paper we assume a circular orbit resulting in a constant v_{orb} . To calculate the rotation and orbital speeds we assume a tidally locked planet ($P_{orb} = P_{rot}$) with an orbital period of 3.53 days. Figure 4 shows the Doppler-shifted wind speeds along the planet’s terminator that result from each of the four atmospheric dynamic models described in Section 2.1. The opacity κ from Equation 2 is finally evaluated at wavelength

$$\lambda = \lambda_0 \left(1 - \frac{v_{LOS}}{c}\right), \quad (5)$$

where λ_0 is the unshifted wavelength, to produce the properly Doppler-shifted absorption.

High resolution spectroscopy at a spectral resolution of $\sim 10^5$ along with sufficiently high signal-to-noise is necessary to measure Doppler shifts in transmission spectra at the km s^{-1} level. Here we calculate all of our transmission spectra at a spectral resolution of 10^6 , which is higher than the resolution of most currently available high-resolution spectrographs by at least an order of magnitude. (For example, the CRIFRES spectrograph used by Snellen et al. (2010) has a working resolution of $\sim 10^5$). We compute spectra at such high resolution to clearly show the effects of Doppler shifts on our transmission spectra and also to show the power of very high spectral resolution for future instrumentation. All of our spectra can be easily degraded to lower spectral resolution by convolution with a Gaussian of the appropriate width.

We calculate all of our spectra from 2291 to 2350 nm as a representative wavelength range over which high resolution transmission spectra can be obtained from the ground. This wavelength range covers the $2.3 \mu\text{m}$ first overtone ($\Delta\nu = 2$) band of CO. This is

also the wavelength coverage of the observations by Snellen et al. (2010), which facilitates comparisons between our model spectra and their results.

It is important to note that the stellar spectrum experiences velocity shifts of its own during transit. These shifts result from both the induced motion from the planet’s orbit (stellar radial velocity) along with the Rossiter-McLaughlin effect by which the planet blocks out a portion of the blue- or red-shifted limb of the star during transit. Both effects produce a zero net Doppler shift at the center of transit, provided that the planet’s orbit is circular and the stellar spin axis is aligned with the normal axis of the planet’s orbit. However, when either of these effects becomes non-zero, it is necessary to divide out the appropriately Doppler-shifted stellar spectrum from the in-transit spectrum to obtain a transmission spectrum that only has the effects of the planetary Doppler shift imprinted on it. For the spectra that we present in the following section, we assume that the stellar Doppler shift is known and has been appropriately accounted for.

3. Results

3.1. Transmission Spectrum Doppler Shifts

The entire 2291-2350 nm section of the hot Jupiter transmission spectrum for the drag-free atmosphere model is shown in Figure 5 with no velocity shifts. In the unshifted spectrum, the first overtone band of CO is clearly visible at the model spectral resolution of 10^6 . Many additional spectral features from water are also present in this region of the spectrum along with weaker CH₄ features that originate from cooler regions in the atmosphere. The comb of strong and well-separated CO lines around 2.3 microns is particularly useful for measuring Doppler shifts as long as the spectral resolution exceeds $\sim 10^4$. At the much lower spectral resolution of most transmission spectrum measurements to date, the 2.3 μm CO features are unresolved in a single broad absorption band, and RV measurements at a precision of ~ 1 km s⁻¹ are not possible.

Figure 6 shows a representative 2.3 nm segment of the fully Doppler shifted spectra from 2308.0 to 2310.3 nm. (The rest of the spectrum shows similar RV shifts from winds, but it is not feasible to show the entire spectral range of our model in a single plot and to still see the Doppler shifts by eye.) A net blueshift in all four models is clearly apparent in the top panel of Figure 6. Additionally, a significant amount of line broadening occurs in the transmission spectra from the joint effects of winds and rotation, which effectively weakens the peak strength of each of the individual spectral lines and also causes many of the adjacent lines to blend together. The effect of broadening due to rotation alone is

shown in the bottom panel of Figure 6, clearly indicating the extent to which the Doppler broadening is due to rotation as opposed to winds. Rotation is the dominant source of broadening (quite similar to the effect of rotational broadening on stellar spectra). However, the winds themselves also cause some further broadening of the transmission spectra, since the wind patterns are not entirely coherent and instead some considerable variation in the line-of-sight wind speeds occurs around the terminator as shown in Figure 4. Some of the models clearly show a higher level of incoherence in the wind pattern than others (e.g. the standard drag-free model as opposed to the model with enhanced hyperdissipation), which has a small effect on the width of the broadened spectral lines from model to model.

By cross correlating the Doppler-shifted spectra against the unshifted transmission spectra, we can obtain the average velocity shift for the entire 2291-2350 nm region of the calculated spectrum. The cross correlation functions for each of the four atmosphere models taken at the center of transit (phase $\varphi = 0$) are shown in Figure 7. Each model gives a different overall velocity shift with the magnetic drag models producing the smallest shifts and the drag-free models producing the largest shifts. The net blueshifts for the drag-free, drag-free with added hyperdissipation, and magnetic drag models (a) and (b) are respectively 2.07, 2.25, 1.33, and 0.99 km s⁻¹. The shifts are as expected with the highest drag models producing the lowest net velocity shifts. However, given that the difference in the magnitude of the Doppler shifts between models only varies by 1.25 km s⁻¹, observations with RV precision of better than 1 km s⁻¹ will be necessary to differentiate between atmospheres with and without magnetic drag. At the 1 km s⁻¹ RV precision of the Snellen et al. (2010) measurements, all four of our model atmospheres are consistent with the measured winds in HD 209458b’s atmosphere of 2 ± 1 km s⁻¹.

It is interesting to note that even though the drag-free model has higher maximum wind speeds than the drag free + hyperdissipation model, the largest Doppler shifts take place in the latter case. This is because the extra hyperdissipation reduces the small-scale numerical noise observed in the original model and results in a more coherent flow. Although the average wind speed across the terminator is the same in both models, the winds are more well aligned in the drag free + hyperdissipation model and contribute more strongly to the blue shifted signal. Although the effect is small, on the order of ~ 200 m/s, this demonstrates the observational uncertainty associated with the choice of hyperdissipation strength in our 3-D models.

When the effects of winds are ignored and only the RV effect of rotation is considered, a zero net Doppler shift is expected because the blueshifting of the eastern limb of the planet should counteract the redshifting of the western limb, resulting in Doppler broadening but no net shift. However, cross-correlating the rotationally broadened spectra against the unshifted

spectra (not shown), results in a small *redshift* for all of our models of $\sim 100 \text{ m s}^{-1}$. This results from the fact that the eastern (blueshifted) limb of the planet tends to be hotter and therefore more puffed up than the western limb. Absorption along the terminator on the cooler limb therefore takes place at longitude angles where $\sin \theta$ is closer to 1.0, which results in the rotation velocity having a larger component along the observer’s line of sight according to Equation 4. As a consequence, the redshifted limb plays the dominant role in the rotational broadening signature. This effect, while interesting, requires measuring the rotational asymmetry in the transmission line profiles at a RV precision that is an order of magnitude higher than what has previously been obtained by Snellen et al. (2010). Even if this were possible, it would be nearly impossible to disentangle the rotational Doppler shifts from the Doppler shifts that result from the planet’s winds.

3.2. Constraints from Ingress and Egress

Currently, measurements of Doppler shifted winds via transmission spectroscopy require that the transmission spectra be integrated over the full transit just to attain the signal-to-noise necessary for making a 1 km s^{-1} measurement. However, future observations that can measure Doppler shifts as a function of orbital phase throughout transit will be a very powerful tool for resolving the spatial structure of the winds across a planet’s terminator. These types of measurements will likely necessitate next generation ground-based 30-m class telescopes to attain high signal-to-noise over shorter exposure times. Of particular interest is the measurement of Doppler shifts during transit ingress and egress when only one limb of the planet is in front of the star, which will allow for a straightforward mapping of the eastward and westward flows on either limb of the planet.

We calculate Doppler shifts as a function of orbital phase throughout transit for each of the four model atmospheres in Figure 8. We separately show the cumulative effects of rotation, winds, and orbital motion. Generally, the orbital motion is the dominant effect on the Doppler-shifted signal. When that motion is subtracted off, as in Snellen et al. (2010), the effects of winds become apparent.

Some details of the calculation resulting in Figure 8 are as follows. Throughout the analysis we use a single snapshot from each model, safely assuming that the amount of temporal variation is negligible and its effect is small compared to our other simplifying assumptions. We account for rotation of the planet away from phase $\varphi = 0$ by shifting the longitudes in our model by an angle equivalent to the orbital phase. This step is important because the planet rotates by an angle of 16° over the duration of the transit relative to an observer on Earth, whereas the frame of reference of the model atmosphere calculations

always has the 0° line of longitude at planet’s substellar point. The planet’s rotation relative to the observer has only a small effect on the calculated velocities, but the effects of the slow eastward motion of both the hottest and coldest points on the planet does induce small velocity shifts throughout transit. For simplicity, we assume that the planet transits exactly across the middle of the star at an orbital inclination of 90° . We do not include any effects of limb darkening. We also ignore the geometric effects of curvature on the limb of the star, in effect treating the edge of the star as a straight line, tangential to the orbital direction of the planet. These last three effects should minimally impact the results shown in Figure 8, but the qualitative results are still instructive.

During full transit, between the 2nd and 3rd contact points when the planet is completely in front of the star, the wind and rotation RVs are fairly constant, despite a very small effect from the rotation of the planet relative to the observer, which can cause shifts of up to 200 m s^{-1} . In contrast, the orbital RV signature varies considerably during transit as it sweeps out the $\varphi = 0$ region of a sine curve with peak amplitude 146 km s^{-1} , equivalent to the orbital speed of the planet on its circular orbit.

However, during transit ingress and egress, between the 1st and 2nd, and 3rd and 4th contact points respectively, the induced Doppler shifts from winds and rotation both vary considerably as first one limb of the planet and then the other appears/disappears in front of the stellar disk. The effect of the planet’s rotation is to blueshift the eastward limb and redshift the westward limb of the planet, thus creating an anomalous redshift during ingress and blueshift during egress. Since the rotation is symmetric, the rotational RV signature is also approximately (anti-)symmetric about the center of transit. The magnitude of the Doppler shift due to rotation alone increases from $\sim 0 \text{ km s}^{-1}$ during the phase of full transit to $\sim 2 \text{ km s}^{-1}$ at the very beginning of ingress and end of egress, which is equivalent to the rotational speed of the planet, as seen in the bottom panel of Figure 8.

Winds display a similar behavior as rotation during ingress and egress where the eastward limb tends to be more strongly blueshifted than the westward limb. This effect varies from model to model and also becomes stronger with depth, as shown in Figure 4. In general, most of the terminator is predicted to be blueshifted at mbar pressures. However, the models with magnetic drag tend to have more uniform velocities, whereas the drag-free models show a stronger tendency towards blueshifted winds at the eastern terminator and redshifted winds at the western terminator. In terms of the ingress and egress velocities, the canonical drag-free model gives the largest differences between the Doppler shifts from winds at the start and finish of transit. At the very beginning of ingress the drag-free model gives an additional 1.6 km s^{-1} blueshift on top of the 2 km s^{-1} redshift from the planet’s rotation (for a net redshift of 0.4 km s^{-1}). At the very end of egress this same model gives an additional

3.3 km s⁻¹ blueshift on top of the 2 km s⁻¹ rotational blueshift. This results in an overall 1.7 km s⁻¹ measured difference between the line-of-sight wind speeds for opposing limbs of the planet. In contrast, the winds in the models with magnetic drag each only produce a 0.2 km s⁻¹ difference in the Doppler shifts between the leading and trailing limbs. If this effect can be measured, it allows for another constraint to be placed on the amount of drag present in a hot Jupiter atmosphere. It serves pointing out that correctly measuring the Doppler shifts that arise exclusively from winds requires that both the orbital and rotational effects be subtracted off, which necessitates an assumption of tidal locking along with knowledge of the orbital speed.

Measuring velocity shifts during ingress and egress faces two key challenges. The first, which has already been mentioned, is that high signal-to-noise spectra must be obtained using fairly short exposures since transit ingress/egress may only each last for 10-30 min in total. A second major challenge to obtaining high signal-to-noise during ingress/egress is that the excess absorption from the planet’s atmosphere that creates the transmission spectrum decreases in magnitude as the planet moves off of the stellar disk. The amount of excess absorption scales linearly with the cross sectional area of atmosphere that is in front of the star at a given time, which quickly reduces to zero at the beginning and end of transit. With almost no photons passing directly through the planet’s atmosphere near 1st and 4th contact, it will be impossible to measure any meaningful Doppler shifts, even if the winds at the edge of the planet’s limb are particularly strong. Doppler shift measurements during ingress/egress should still be possible when a larger fraction of the planet is in front of its host star, but the signal-to-noise requirements will almost certainly require next generation telescopes and instrumentation.

3.3. Constraints from Individual Spectral Lines

Another interesting constraint can be placed on the spatial structure of the winds by measuring Doppler shifts from individual spectral lines. Stronger spectral lines in transmission result from the planet becoming optically thick at larger radii, so these lines originate higher in the atmosphere. Therefore, by measuring velocity shifts in individual spectral lines as a function of their peak strength, a measurement can be made of the vertical structure of the exoplanet winds. If stronger lines produce larger Doppler shifts, then the winds higher in the atmosphere are stronger, whereas weaker Doppler shifts at altitude imply that wind speeds fall off as a function of height.

Our drag-free atmosphere models tend to produce higher line-of-sight wind speeds at altitude, whereas the magnetic drag models have very little wind shear or even opposite wind

shear in the case of magnetic drag model (b) (see Figure 4). To test the extent to which this could be an observable effect, we determine Doppler shifts for 134 individual spectral lines relative to their rest wavelengths. The results for each of the four atmosphere models are shown in Figure 9. As predicted, the drag-free models show increasing velocity (blue) shifts as a function of increasing line strength, whereas magnetic drag model (a) shows almost no RV variation as a function of height, and model (b) produces a slight trend towards decreasing velocity shifts at altitude. The line shifts were all calculated by measuring the shift in the wavelength of peak intensity from the unshifted model to the fully Doppler shifted model. For this reason, velocity shifts are only measured in integer multiples of the velocity resolution of our $R = 10^6$ spectra, resulting in the vertical alignment seen amongst groups of data points in Figure 9.

Linear fits to the line shift data for each model are also shown in Figure 9 to guide the eye, as there is considerable scatter in the measurements. The 134 lines sampled include spectral lines from CO, H₂O, and CH₄, which likely increases the scatter in the line strength vs. velocity relationship. This is particularly true for CO and CH₄ because lines from these two molecules tend to originate from different regions of the atmosphere – CO from regions of hotter gas, likely weighted towards the eastern terminator and CH₄ from regions of colder gas on the western terminator. Measuring the line strengths for only the 76 first-overtone lines of CO (not shown) results in a tighter linear relationship for line strength vs. velocity. However, this particular set of lines samples a far smaller range of altitude in the atmosphere, since all of the CO spectral lines are quite strong and therefore originate from regions of high altitude and low pressure.

Measuring Doppler shifts of individual spectra lines in transmission is another effect that will almost certainly require next generation instrumentation to realize, due to the very high signal-to-noise requirements. The only measurements of Doppler shifts in transmission to date (Snellen et al. 2010) required the full spectrum from 2291 to 2349 nm to detect a Doppler shift at km s⁻¹ precision. Individual spectral lines were not present in their spectra at close to sufficient signal-to-noise to measure RV shifts, even when integrating over a full transit.

4. Summary / Conclusion

We have coupled together an existing 3-D atmospheric dynamics model with a transmission spectroscopy radiative transfer code to study the effects of Doppler shifted winds (along with rotation and orbital motion) on the transmission spectra of hot Jupiter exoplanets. We find that day-to-night winds at altitudes of $\lesssim 1$ mbar can produce significant blueshifts

in hot Jupiter transmission spectra at the level of 1-2 km s⁻¹. Also, the combined effects of winds and the planet’s rotation lead to considerable Doppler broadening of the spectral lines beyond what is predicted if no Doppler shifts are included. These effects all become important for transmission spectra taken at high spectral resolution of $R \gtrsim 10^5$. We have explored different prescriptions for magnetic drag in the atmospheres of hot Jupiters, and we find that the models with the largest amount of magnetic drag produce the slowest wind speeds and therefore the smallest Doppler (blue) shifts, while the models with no magnetic drag produce the largest velocity shifts. In our modeling, the magnetic drag models produce net blueshifts of ~ 1 km s⁻¹, whereas the models with no drag produce blueshifts of ~ 2 km s⁻¹. Ultimately differentiating between different drag prescriptions through observations of hot Jupiter transmission spectra will therefore require RV precision of much higher than 1 km s⁻¹. In the meantime, the current measurement of a 2 ± 1 km/s blueshift in HD 209458b’s transmission spectrum by Snellen et al. (2010) remains consistent with models both with and without magnetic drag.

Still, the results of our modeling give considerable credence to the interpretation that the blueshift observed in HD 209458b’s transmission spectrum results from high altitude winds, as our models produce Doppler shifts of exactly that size. An intriguing alternate interpretation of the Snellen et al. (2010) observed blueshift has been proposed by Montalto et al. (2011), who show that a small eccentricity in the orbit of HD 209458b can also produce a net blueshift in the planet’s transmission spectrum from orbital motion alone. The eccentricity of HD 209458b’s orbit is strongly constrained and consistent with zero (Winn et al. 2005; Deming et al. 2005). However, using the 3- σ upper limits on the planet’s eccentricity, Montalto et al. (2011) find that a blueshift of up to 1 km s⁻¹ could result from a non-circular orbit, which is consistent with the Snellen et al. (2010) observed velocity shift within its error bars. Ultimately, better constraints on the orbital eccentricity of HD 209458b will be needed to resolve whether winds or a non-circular orbit are the cause for the observed blueshift in the planet’s spectrum. In the meantime, a probable very low eccentricity for HD 209458b does require that winds play the dominant role in producing km s⁻¹ blueshifts in the planet’s transmission spectrum.

Even more ambitious observations aimed at spatially resolving exoplanet winds by observing Doppler shifts for individual spectral lines and Doppler shifts as a function of transit phase will likely remain beyond the reach of current observational facilities. Future instrumentation – high resolution spectrographs with $R \gtrsim 10^5$ on next generation 30-m class telescopes – may be able to measure some of these effects. A combination of vertical wind shear measurements obtained from the Doppler shifts of individual spectral lines along with ingress and egress measurements of wind speeds on opposing limbs of the planet can produce a 3-D “map” of winds along an exoplanet’s terminator. This is of particular interest

for tidally locked hot Jupiters, since the winds at the terminator are intimately tied to the day-to-night heat flow and therefore to the global energy budget of the planet.

We caution that the form for magnetic drag used in these 3-D models is simplistic and a more realistic treatment could result in a different flow pattern, which would alter the details of the predicted ingress/egress and vertical shear measurements. However, with these models we have been able to demonstrate the types of observations that would constrain the 3-D atmospheric circulation. Regardless of the exact form for the magnetic drag, what *is* a fairly robust result is that the drag should work to reduce wind speeds, resulting in smaller Doppler shifts in the observed spectra.

In a particularly interesting proof of concept, Hedelt et al. (2011) observed the transmission spectrum of Venus during its 2004 transit of the Sun and discovered Doppler shifted spectral line profiles. While many differences exist between Venus and hot Jupiters, the very slow (retrograde) rotation of Venus means that it has very long days (~ 0.5 Venus years), compared to hot Jupiters' permanent days, resulting in some similarities between their circulation regimes. A full analysis of Venus' Doppler shifted line profiles is beyond the scope of the Hedelt et al. (2011) paper, but the authors comment that the observed Doppler shifts likely result from a combination of super-rotation of Venus' mesosphere along with day-to-night flow – similar to what we predict for hot Jupiter atmospheres but at lower velocities. Using spatially resolved spectra, Hedelt et al. (2011) were furthermore able to separately measure the wind speeds on both the leading and trailing limbs of the planet and also to directly measure the vertical wind shear. The high resolution and high signal-to-noise transmission spectra obtained by Hedelt et al. (2011) show the power of using transmission spectroscopy to constrain the wind patterns in the upper atmospheres of extrasolar planets.

Ultimately, measurements of winds in hot Jupiter atmospheres will be able to constrain the circulation and flow patterns in an interesting new regime. The flow patterns that are expected to result from the tidal locking and very hot dayside temperatures of these planets require observational confirmation, and we have laid out some of the methods for modeling and interpreting those observations throughout this paper. The observation of a blueshifted transmission spectrum for HD 209458b by Snellen et al. (2010) was an exciting first step towards observationally constraining the wind patterns on hot Jupiters. Similar observations of a larger number of hot Jupiters will be able to confirm whether the blueshifted line profiles resulting from high altitude day-to-night winds are ubiquitous or vary considerably from planet to planet. This will help to better understand diversity in hot Jupiter circulation (as indicated by differences in planets' thermal phase curves), especially as is related to the effect of magnetic drag, which will depend on a given planet's atmospheric temperatures and magnetic field strength.

Currently, the available instrumentation is a limiting factor in measuring and constraining the wind patterns on hot Jupiters. Next generation instrumentation will allow for higher precision and more detailed measurements to be taken of a larger number of hot Jupiter atmospheres. Combining these observations with the results from theoretical modeling will provide powerful and unique constraints on day-to-night flow on hot Jupiters.

E. M.-R. K and E. R. were supported by contracts with the California Institute of Technology, funded by NASA through the Sagan Fellowship Program. We thank Paul A. Kempton for his design and collaboration on Figure 4. We thank Kristen Menou for encouraging this work. Both E. M.-R. K and E. R. also credit the AstroWin 2011 workshop at the University of Florida for hosting us and encouraging the collaboration the resulted in this paper.

REFERENCES

- Burrows, A., Rauscher, E., Spiegel, D. S., & Menou, K. 2010, *ApJ*, 719, 341
- Cowan, N. B., Agol, E., & Charbonneau, D. 2007, *MNRAS*, 379, 641
- Crossfield, I. J. M., Hansen, B. M. S., Harrington, J., Cho, J. Y.-K., Deming, D., Menou, K., & Seager, S. 2010, *ApJ*, 723, 1436
- Deming, D., Seager, S., Richardson, L. J., & Harrington, J. 2005, *Nature*, 434, 740
- Dobbs-Dixon, I., Cumming, A., & Lin, D. N. C. 2010, *ApJ*, 710, 1395
- Fortney, J. J., Shabram, M., Showman, A. P., Lian, Y., Freedman, R. S., Marley, M. S., & Lewis, N. K. 2010, *ApJ*, 709, 1396
- Harrington, J., Hansen, B. M., Luszcz, S. H., Seager, S., Deming, D., Menou, K., Cho, J. Y.-K., & Richardson, L. J. 2006, *Science*, 314, 623
- Hedelt, P., Alonso, R., Brown, T., Collados Vera, M., Rauer, H., Schleicher, H., Schmidt, W., Schreier, F., & Titz, R. 2011, *ArXiv e-prints*
- Heng, K., Menou, K., & Phillipps, P. J. 2011, *MNRAS*, 413, 2380
- Hubbard, W. B., Fortney, J. J., Lunine, J. I., Burrows, A., Sudarsky, D., & Pinto, P. 2001, *ApJ*, 560, 413
- Iro, N., Bézard, B., & Guillot, T. 2005, *A&A*, 436, 719

- Jensen, A. G., Redfield, S., Endl, M., Cochran, W. D., Koesterke, L., & Barman, T. S. 2011, ArXiv e-prints
- Knutson, H. A., Charbonneau, D., Allen, L. E., Fortney, J. J., Agol, E., Cowan, N. B., Showman, A. P., Cooper, C. S., & Megeath, S. T. 2007, *Nature*, 447, 183
- Knutson, H. A., Charbonneau, D., Cowan, N. B., Fortney, J. J., Showman, A. P., Agol, E., Henry, G. W., Everett, M. E., & Allen, L. E. 2009, *ApJ*, 690, 822
- Menou, K. & Rauscher, E. 2009, *ApJ*, 700, 887
- Miller-Ricci, E. & Fortney, J. J. 2010, *ApJ*, 716, L74
- Miller-Ricci, E., Seager, S., & Sasselov, D. 2009, *ApJ*, 690, 1056
- Montalto, M., Santos, N. C., Boisse, I., Boué, G., Figueira, P., & Sousa, S. 2011, *A&A*, 528, L17+
- Perna, R., Menou, K., & Rauscher, E. 2010, *ApJ*, 719, 1421
- Rasio, F. A., Tout, C. A., Lubow, S. H., & Livio, M. 1996, *ApJ*, 470, 1187
- Rauscher, E. & Menou, K. 2010, *ApJ*, 714, 1334
- Redfield, S., Endl, M., Cochran, W. D., & Koesterke, L. 2008, *ApJ*, 673, L87
- Showman, A. P., Fortney, J. J., Lian, Y., Marley, M. S., Freedman, R. S., Knutson, H. A., & Charbonneau, D. 2009, *ApJ*, 699, 564
- Showman, A. P. & Polvani, L. M. 2011, *ApJ*, 738, 71
- Snellen, I. A. G., de Kok, R. J., de Mooij, E. J. W., & Albrecht, S. 2010, *Nature*, 465, 1049
- Spiegel, D. S., Haiman, Z., & Gaudi, B. S. 2007, *ApJ*, 669, 1324
- Thraustarson, H. T. & Cho, J. Y. 2011, *ApJ*, 729, 117
- Winn, J. N., Noyes, R. W., Holman, M. J., Charbonneau, D., Ohta, Y., Taruya, A., Suto, Y., Narita, N., Turner, E. L., Johnson, J. A., Marcy, G. W., Butler, R. P., & Vogt, S. S. 2005, *ApJ*, 631, 1215

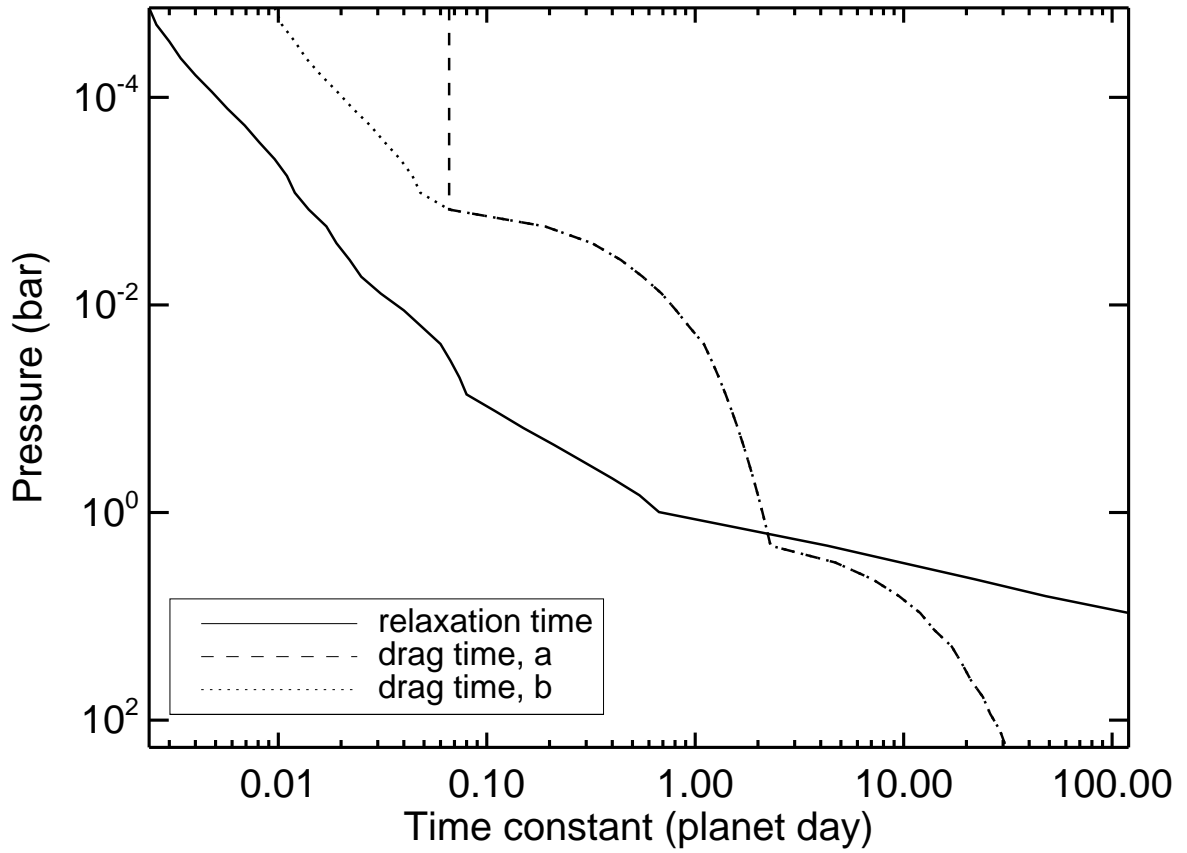


Fig. 1.— Time constants used for the radiative forcing (*solid*) and magnetic drag schemes (*dashed* and *dotted*, two versions). The times are given in units of a planetary day (= orbital period defined as 3.53 d). The radiative times are set to be infinite at pressures greater than 10 bar.

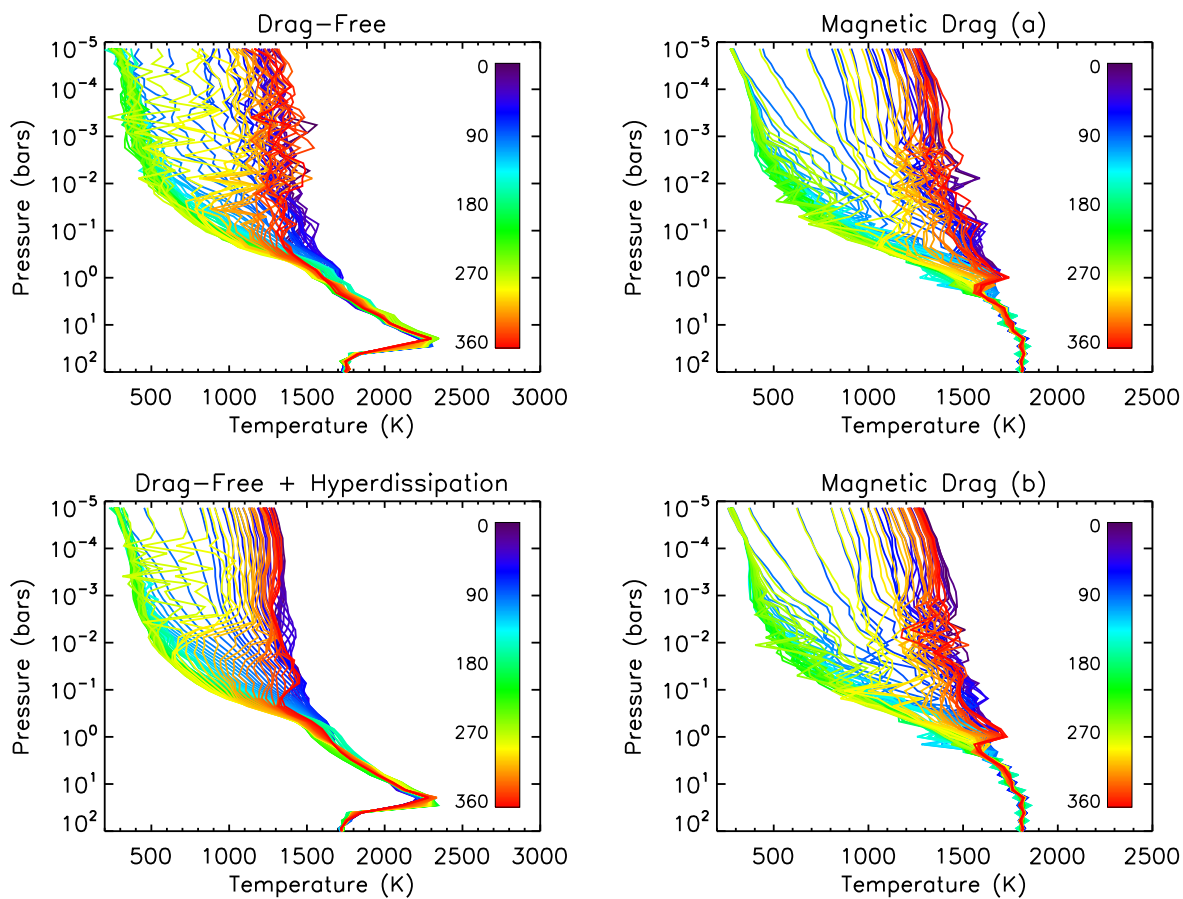


Fig. 2.— Equatorial temperature-pressure profiles for each of the four hot Jupiter models. All profiles are taken at the equator for longitudes from the substellar point ($\theta = 0^\circ$), eastward to the antistellar point ($\theta = 180^\circ$), and back around to the day side as indicated by the line color. The eastward (trailing) limb located at $\theta = 90^\circ$, is hotter than the westward limb for all four models at moderate pressures, which is an effect of eastward advection of hot dayside gas.

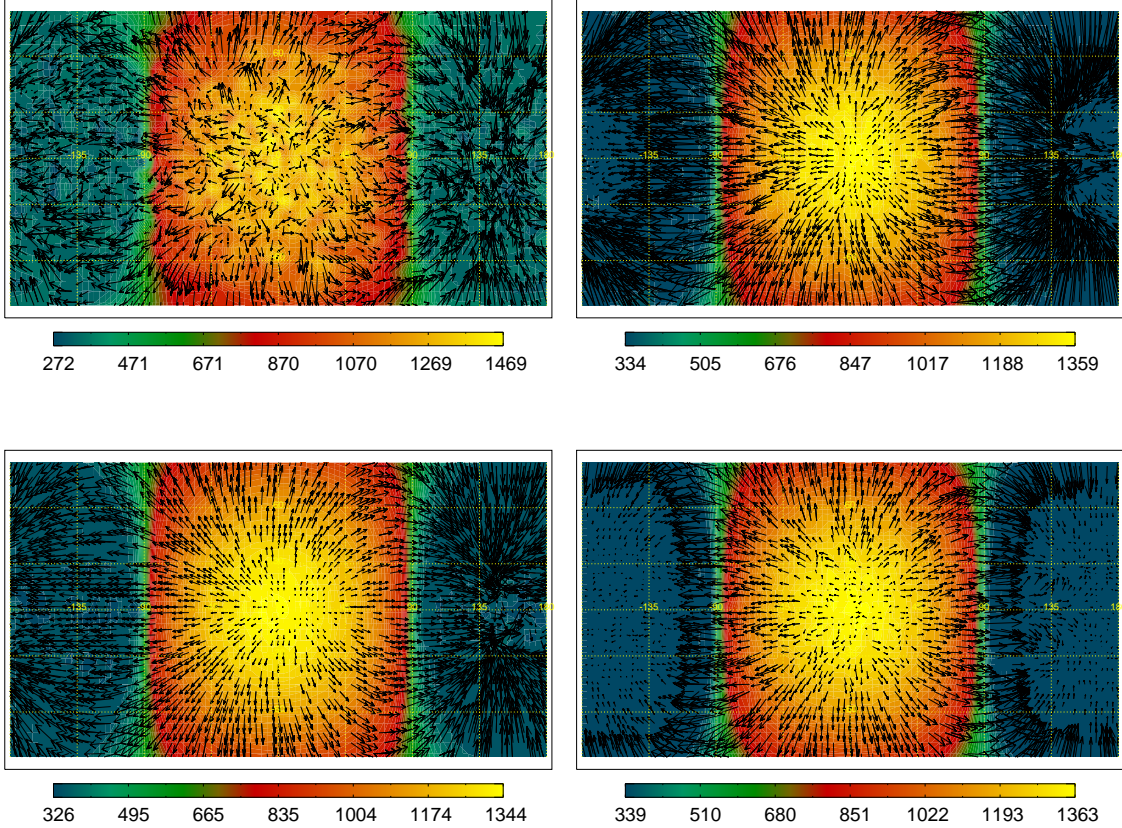


Fig. 3.— Temperature map at the 60 μbar level, with two-dimensional wind vectors over-plotted. (The center of the plot is the substellar point.) Shown are the original drag-free model (*top left*), the drag-free model with enhanced hyperdissipation (*bottom left*), and the magnetic drag models, (a) which assumes τ_{drag} constant above 1 mbar (*top right*), and (b) with $\tau_{\text{drag}}/\tau_{\text{rad}}$ constant (*bottom right*). The maximum wind speeds in each of the models (clockwise from top left) are 15, 4.5, 2.5 , and 11 km/s.

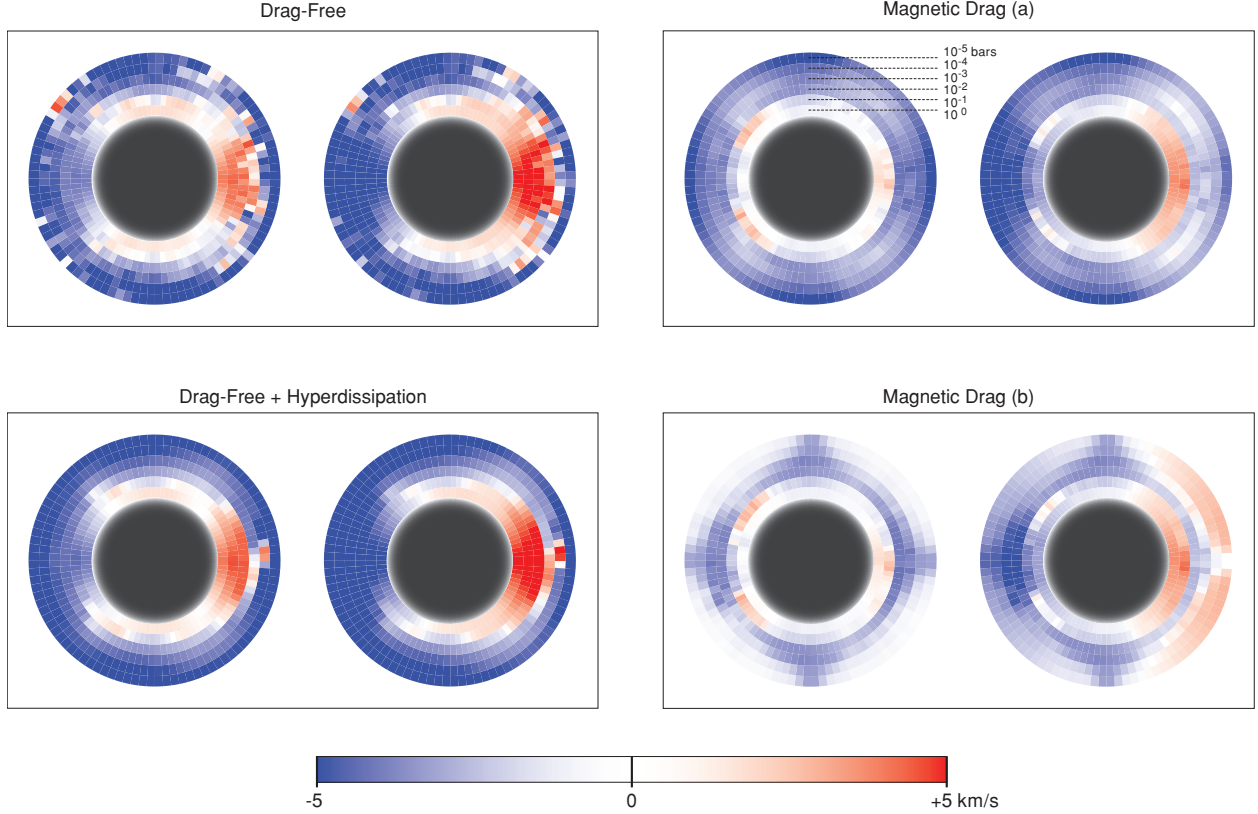


Fig. 4.— Line-of-sight velocities at the terminator for the various models. The left-hand image in each pair shows the line-of-sight wind speeds in the frame of the planet, whereas the right-hand image is in the frame of the observer and includes the effect of the planet’s rotation. All snapshots are taken at orbital phase $\varphi = 0$ where the orbital motion has a null effect on the line-of-sight velocity. The form and strength of hyperdissipation and/or magnetic drag changes the line-of-sight wind speeds as well as the pressures at which they are the strongest. Rotation always blueshifts the east terminator and redshifts the west, at a magnitude of $\sim 2 \text{ km s}^{-1}$ at the equator. Line-of-sight velocities over 5 km s^{-1} are shown in the darkest shade of red/blue.

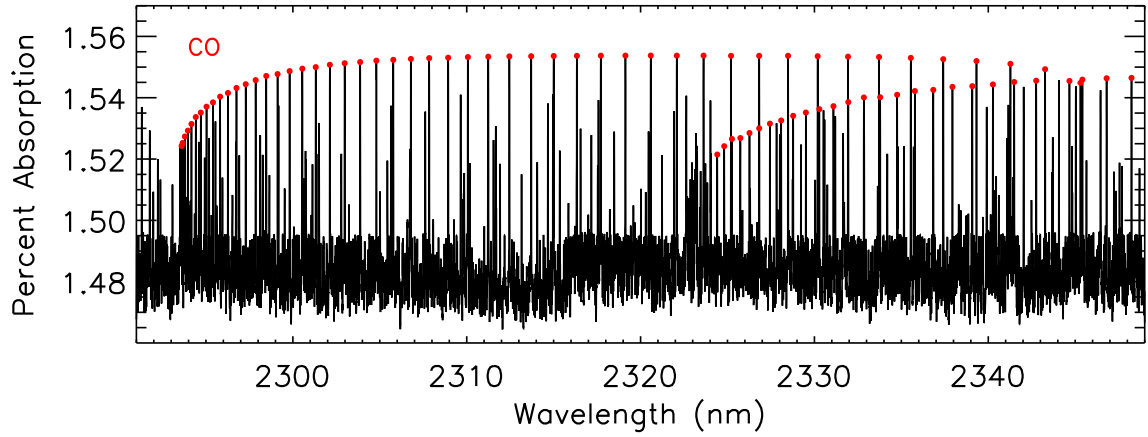


Fig. 5.— Unshifted transmission spectrum calculated from 2291 to 2349 nm. The y-axis plots the transit depth in percent as a function of wavelength. The strong regularly-spaced spectral lines are the $2.3 \mu\text{m}$ first overtone band of CO. (The $\nu = 2 - 0$ and $\nu = 3 - 1$ bands of CO are indicated in red.) The remainder of the absorption lines in this region of the spectrum are mostly from H_2O and CH_4 , with a much smaller number of weak lines from NH_3 .

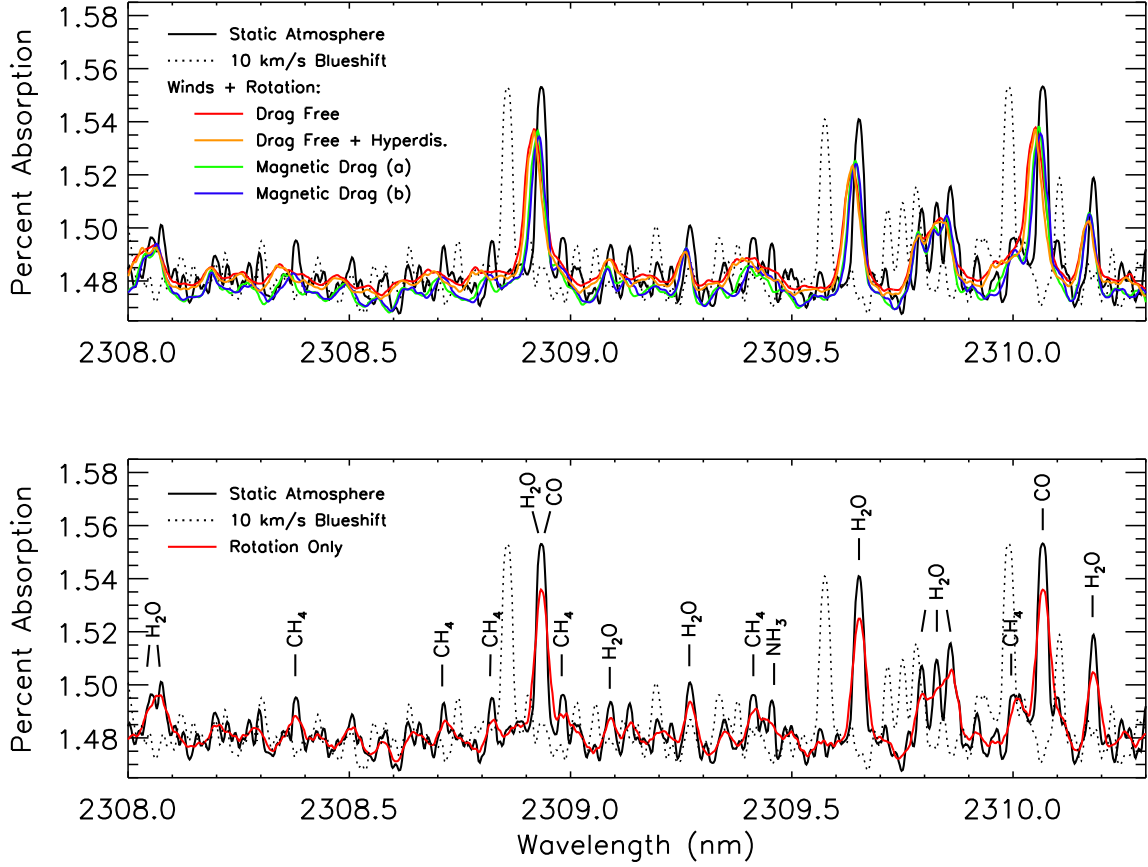


Fig. 6.— Snapshots of a 2.3 nm section of the Doppler-shifted transmission spectra taken at the center of transit ($\varphi = 0$). *Top*: Doppler shifted spectra including the effects of both winds and rotation. All models reveal a net blueshift that varies from 1-2 km s⁻¹ depending on the drag prescription. The unshifted transmission spectrum for the drag-free case is shown (*black solid*), as is the same spectrum with a constant 10 km s⁻¹ offset for reference (*black dotted*). *Bottom*: Same as above but only the effect of rotation is included, which broadens the spectrum but does not induce a significant RV shift. Only the drag-free case is shown, as all four models produce almost identical rotational signatures.

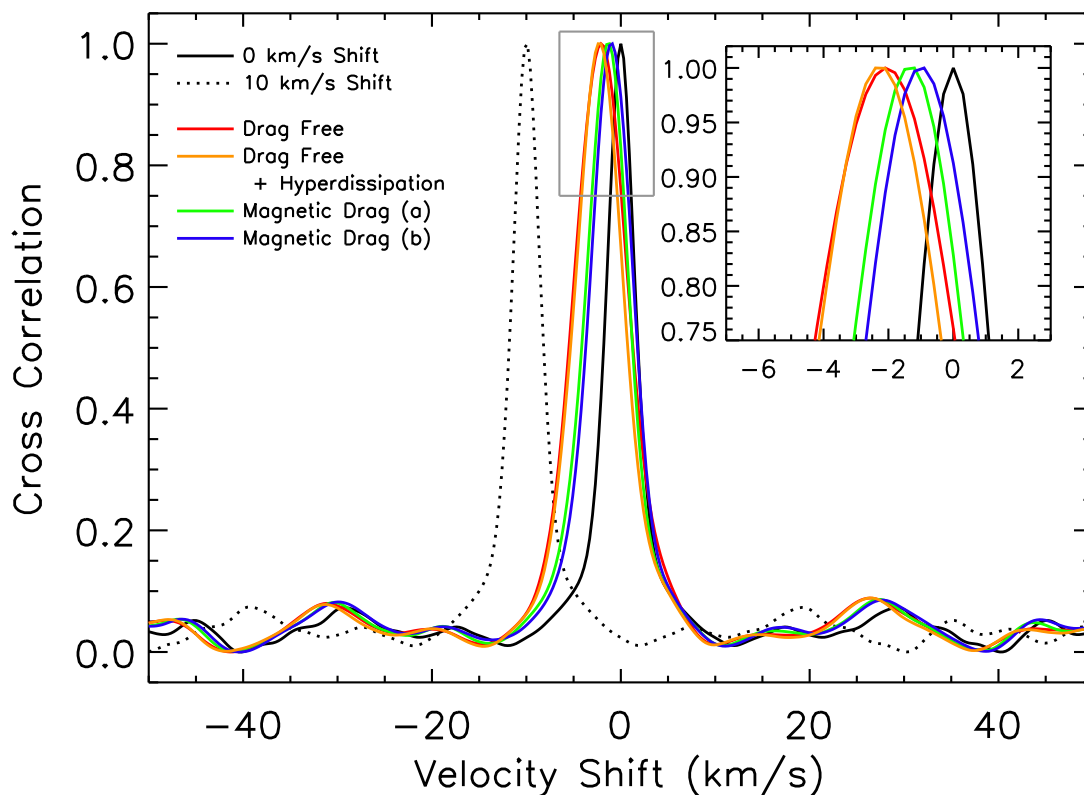


Fig. 7.— Cross correlation functions for each of the four atmosphere models taken at the center of transit against the unshifted spectra. The cross correlation function for the unshifted drag-free spectrum against itself (*black*) and with a 10 km s^{-1} blueshift (*dotted black*) are shown for reference. The strongest RV shifts belong to the models with the weakest drag prescriptions and vice versa.

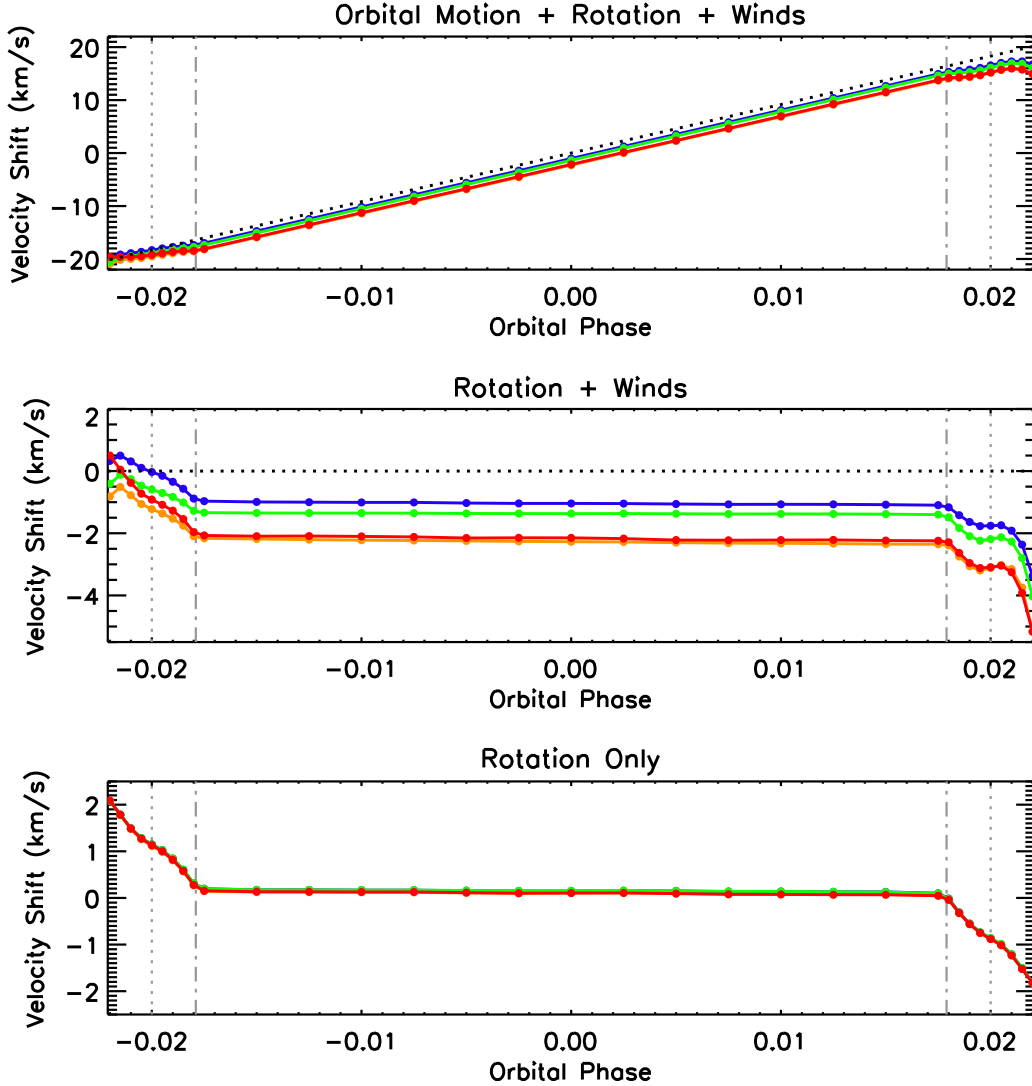


Fig. 8.— Velocity shifts as a function of orbital phase. *Top*: The cumulative RV effects of orbital motion, winds, and rotation are shown. The dotted black line indicates the Doppler shift that would be expected if orbital motion was the only contributor to the RV signal. *Middle*: The cumulative RV effects of winds and rotation. The dotted black curve from the top panel has been subtracted off (now shown as a horizontal line at 0 km s^{-1}), revealing a blueshifted offset for all four models that results from day-to-night winds. *Bottom*: The RV effects of rotation alone. The left-hand and right-hand boundaries of the plots are at the 1st and 4th contacts of transit, and gray vertical dot-dashed lines indicate the 2nd and 3rd contacts of transit, and dotted lines indicate the “1.5th” and “3.5th” contact points where one limb of the planet each is on and off of the star. All effects of limb darkening have been ignored.

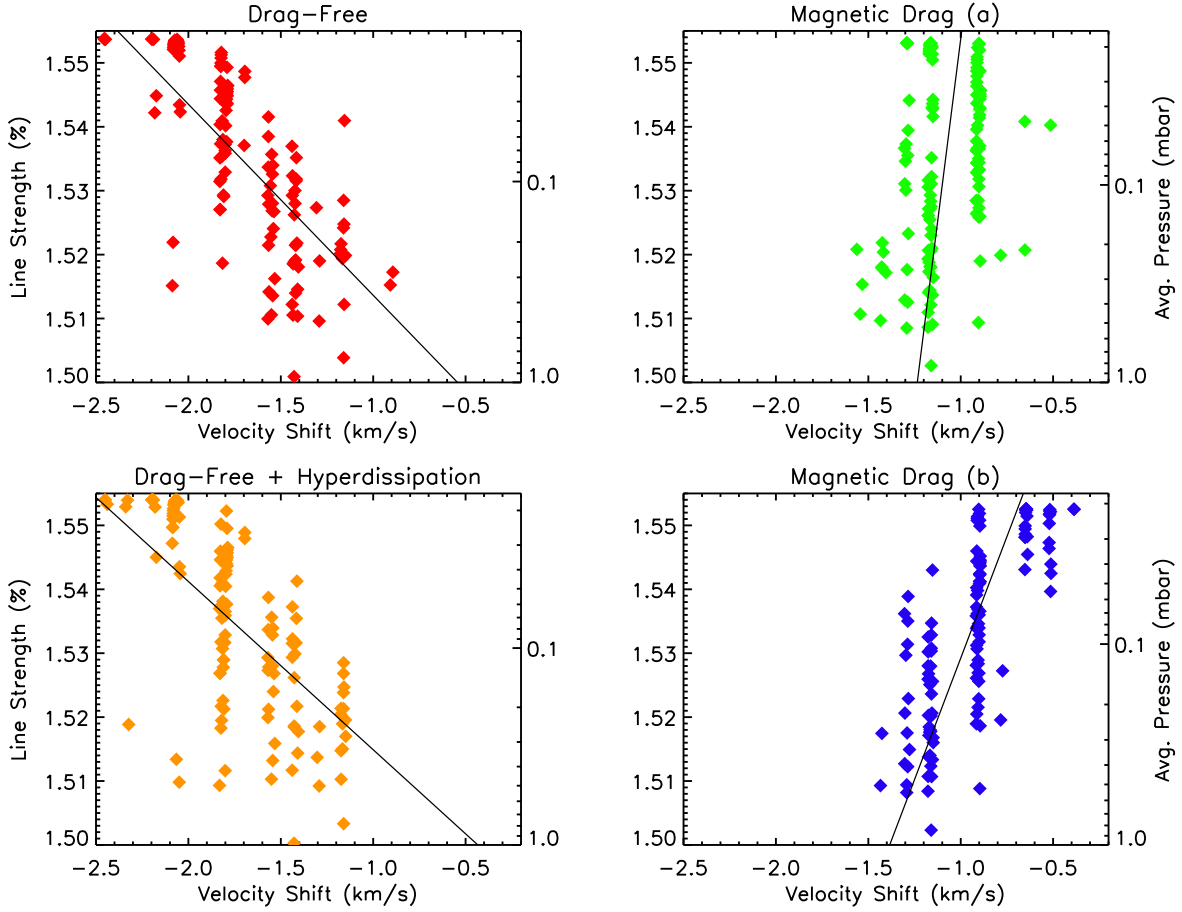


Fig. 9.— Strength of individual spectral lines (i.e. their peak transit depth in percent) vs. Doppler shift. The stronger lines originate from higher in the atmosphere. Shifts for 134 individual lines are plotted with a linear fit overlaid. The average atmospheric pressure corresponding to a given line strength is also indicated. The vertical alignment (striping) in the data is due to the velocity resolution of our $R = 10^6$ spectra.